High-temperature metamorphism and crustal melting: working with melt inclusions

Omar Bartoli[1]*, Antonio Acosta-Vigil[1,2], Bernardo Cesare[1]

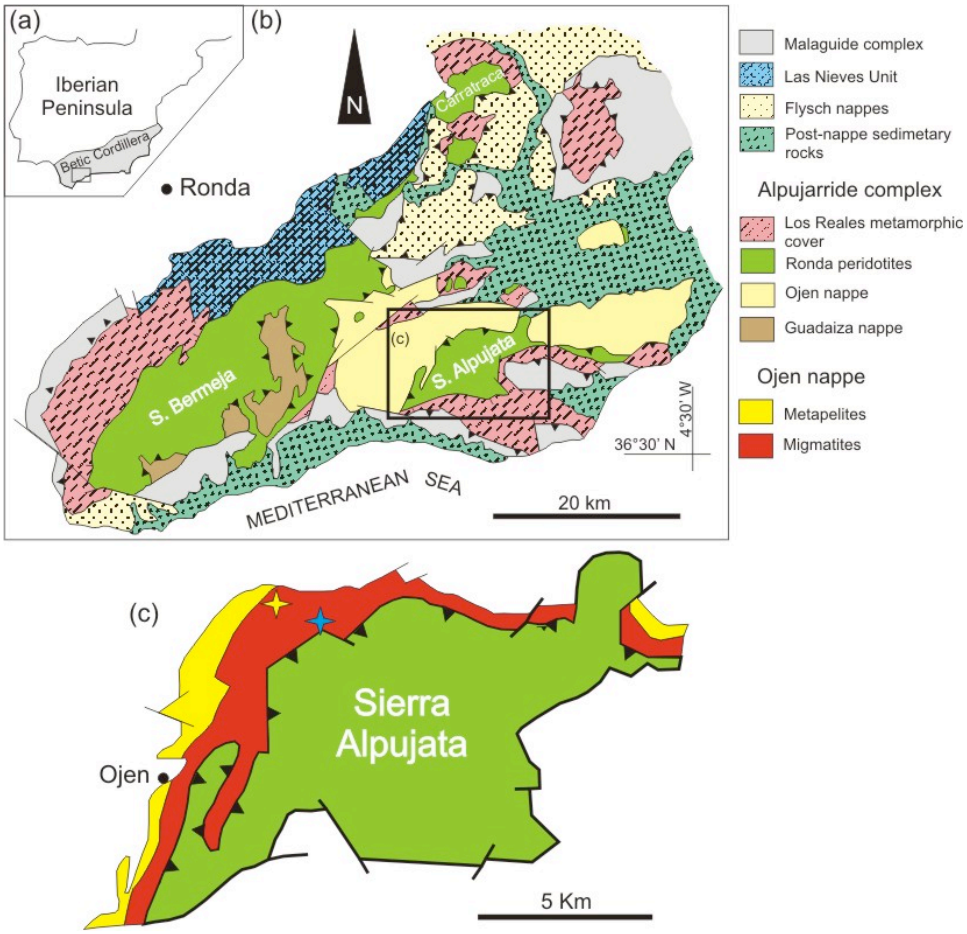

Fig. 1: (a) Location map of the study area in the S Spain. (b) Simplified geological map of the western sector of the Betic Cordillera (modified after Esteban et al., 2011b). (c) Geological map of the Sierra Alpujata massif. Blue and yellow stars show the location of the studied mylonite ALP13 and metatexite ALP1.

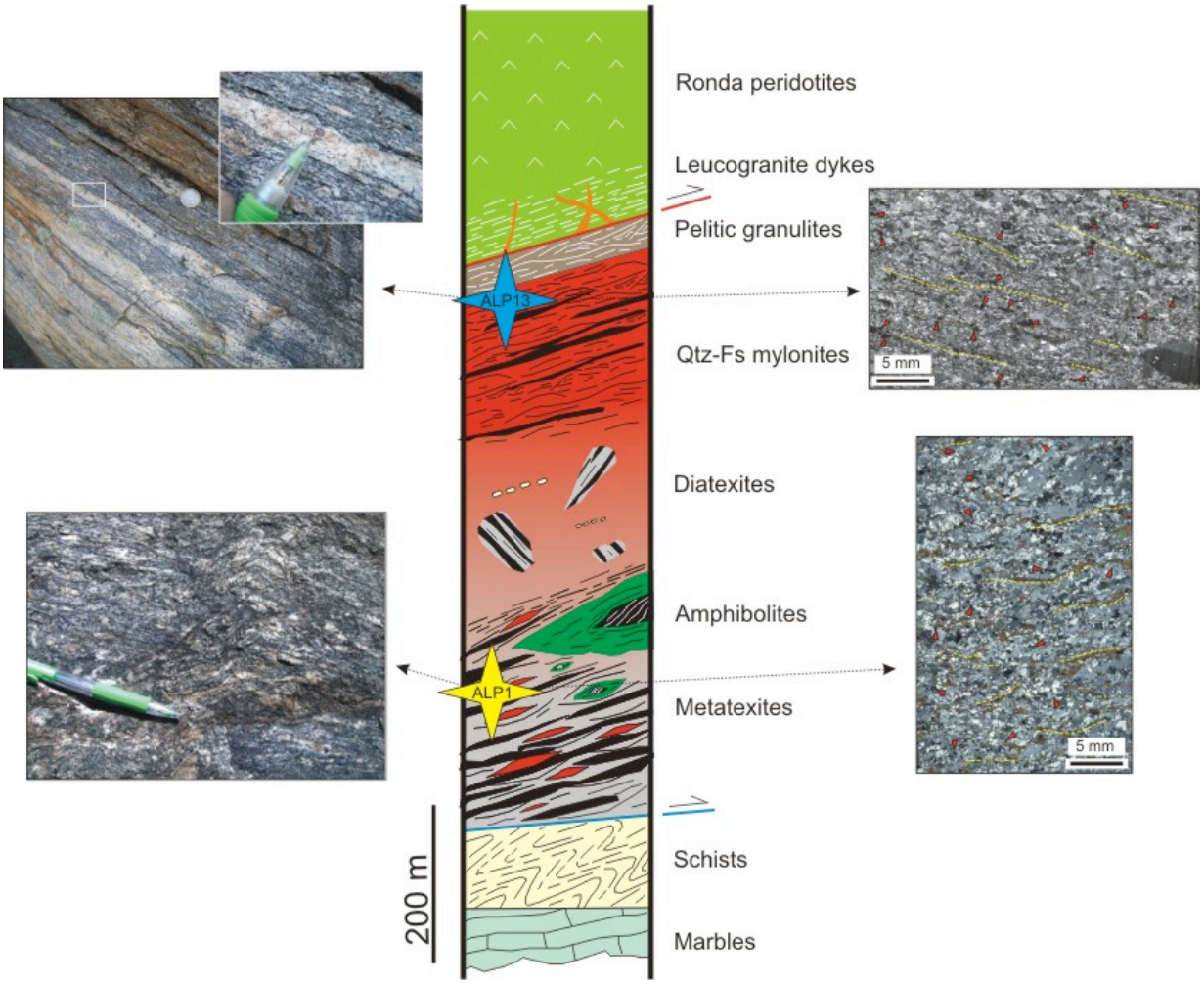

Fig. 2: Schematic section of the crustal footwall of the Ronda peridotites at Sierra Alpujata showing the location of the studied samples (blue and yellow stars as in Figure 1). The field aspect images and photomicrographs show the macro and microstructural evolution of migmatites as a function of distance to the bottom of the Ronda peridotite slab. Red arrows show the location of peritectic garnets. Yellow lines show the traces of the main foliation defined by biotite and/or sillimanite folia.

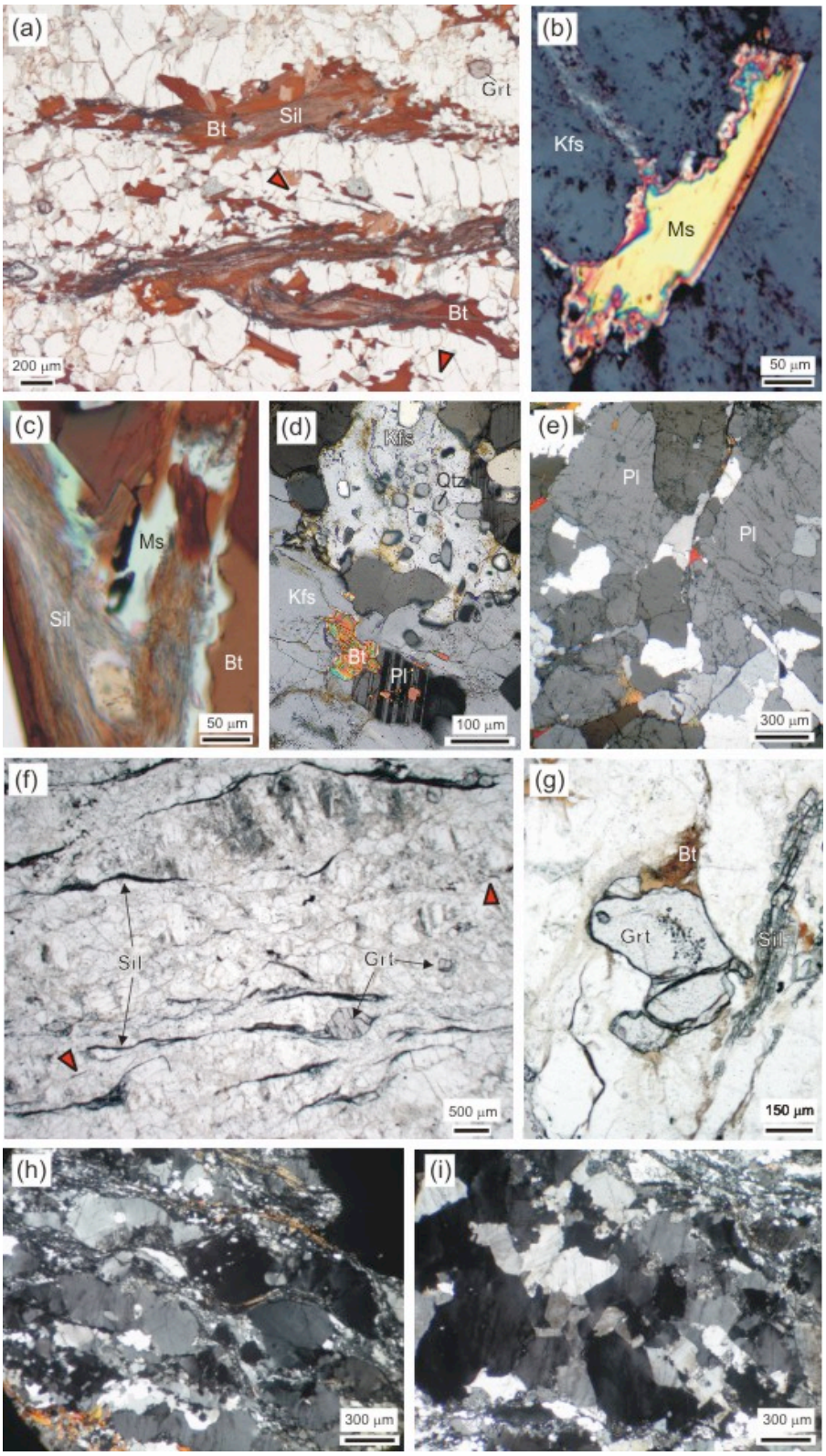

Fig. 3: Microstructures in the stromatic metatexite ALP1 (a-e) and mylonite ALP13 (f-i). (a) Photomicrograph of the mesocratic matrix in which biotite and sillimanite grains define the main foliation. Red arrows: graphite lamellae (b) Resorbed muscovite armoured in K-feldspar porphyroblast. (c) Primary muscovite partially replaced by fibrolite. (d) K-feldspar poikiloblast with inclusions of

quartz, plagioclase and biotite. (e) Euhedral faces of feldspar, suggesting crystal growth from melt (Vernon, 2011) in a leucocratic band. (f) Mesocratic matrix showing fabric-forming sillimanite. Red arrows: graphite lamellae. (g) Garnet crystal partially replaced by Bt formed as product of retrograde reactions during cooling. (h, i) Photomicrographs of two leucocratic bands. In (h) feldspars and quartz are deformed and elongated, whereas they display euhedral shape with planar faces in (i).

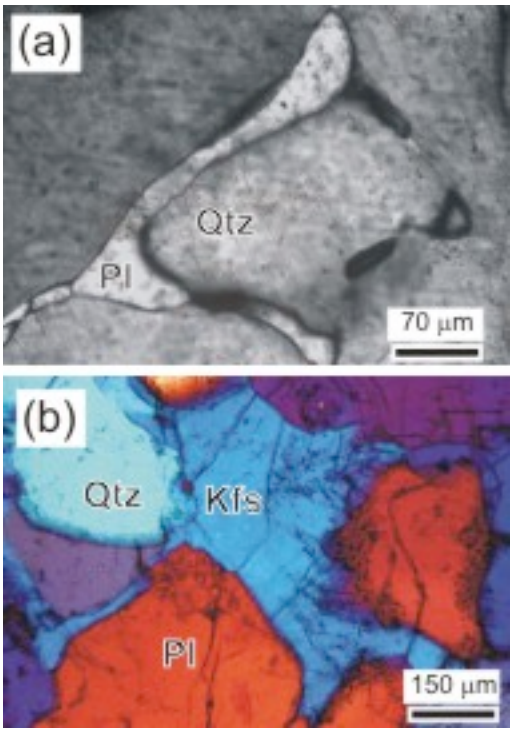

Fig. 4: Photomicrographs of pseudomorphs after melt films in metatexite. (a) Plagioclase that crystallized as a melt pseudomorph around rounded quartz. (b) K-feldspar with cuspate outlines that has probably crystallized from a pool of melt. The reactant minerals, quartz and plagioclase, are rounded and resorbed. Crossed polars with λ plate.

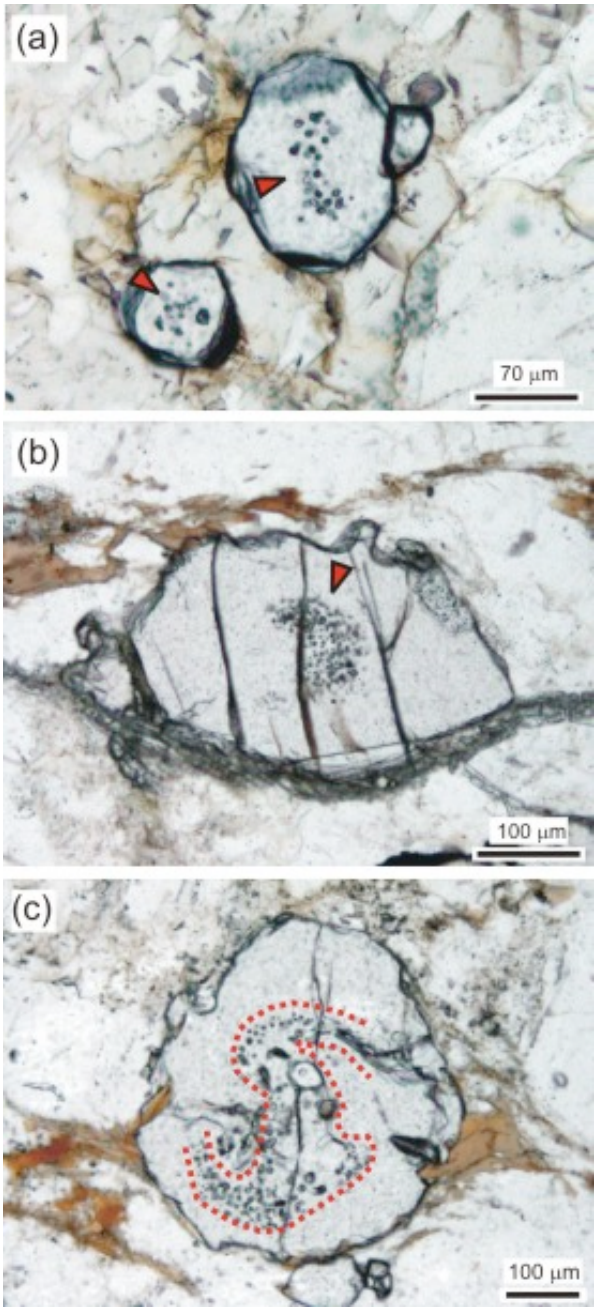

Fig. 5: Photomicrographs of the MI-bearing garnets in metatexite (a) and mylonite (b, c). MI clusters may show a subspherical geometry (red arrows) or a spiral-like arrangement (red dotted lines).

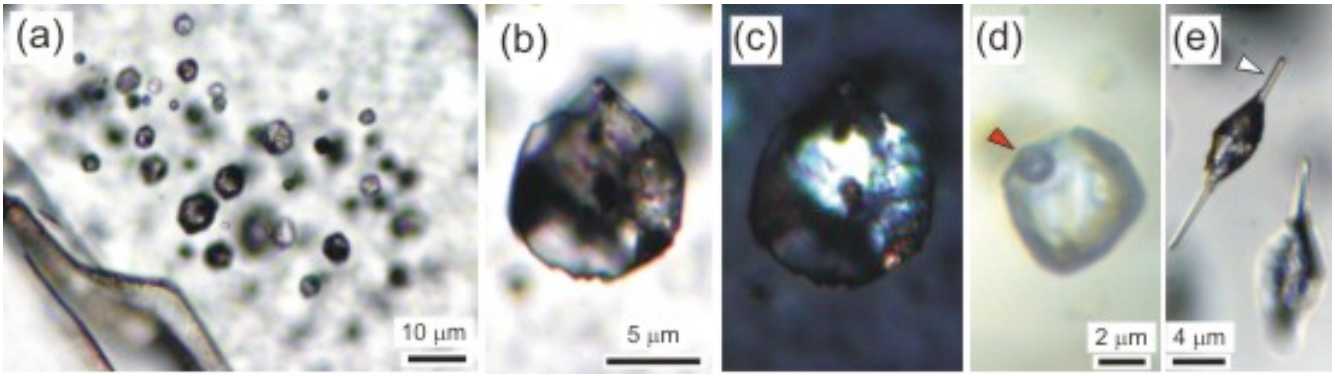

Fig. 6: Photomicrographs of melt inclusions. (a) Plane-polarized image of a MI cluster in metatexite. (b, c) Plane-polarized and crossed polars images respectively of a crystallized inclusion in metatexite. (d) Glassy MI containing a shrinkage bubble (red arrow) in diatexite, plane-polarized light. (e) Crystallized MI with a Sil needle (white arrow) that is likely to have favored the entrapment of melt, plane-polarized light.

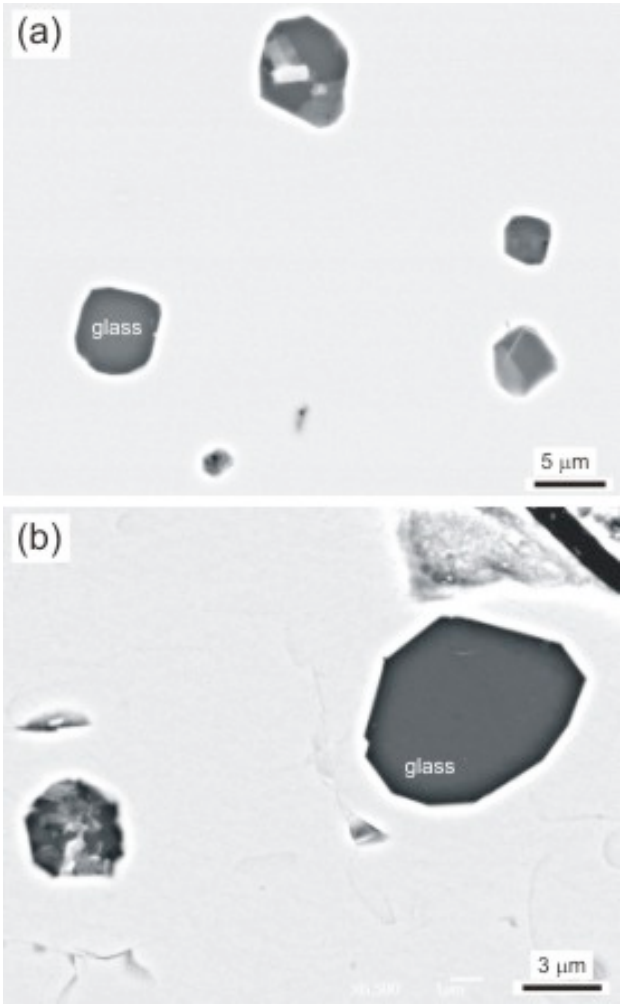

Fig. 7: SEM-BSE images of coexisting crystallized and preserved glassy MI in metatexite (a) and mylonite (b).

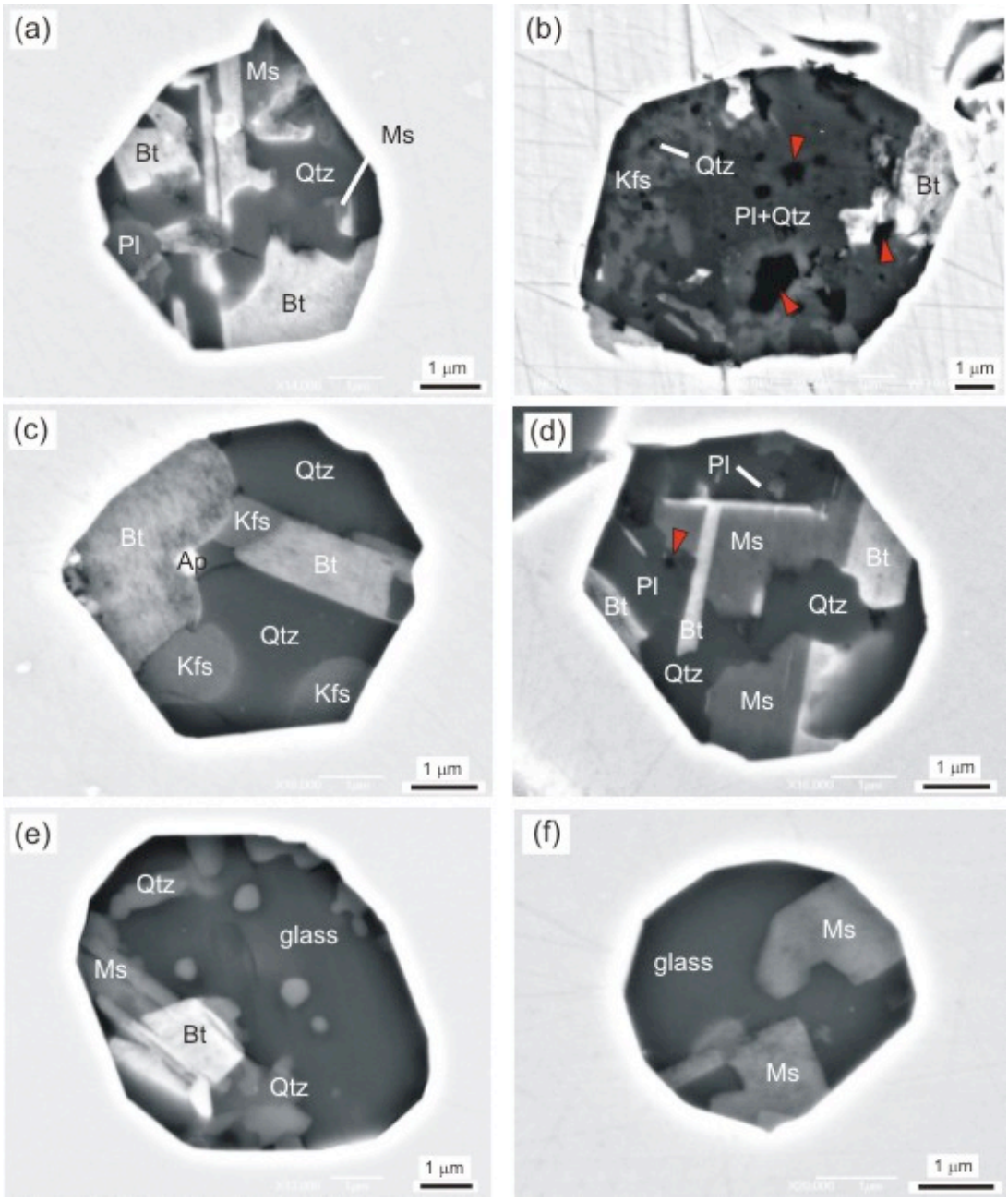

Fig. 8: SEM-BSE images of nanogranites and partially crystalized inclusions in metatexite (a, b, e) and mylonite (c, d, f). Red arrows: primary nanoporosity.

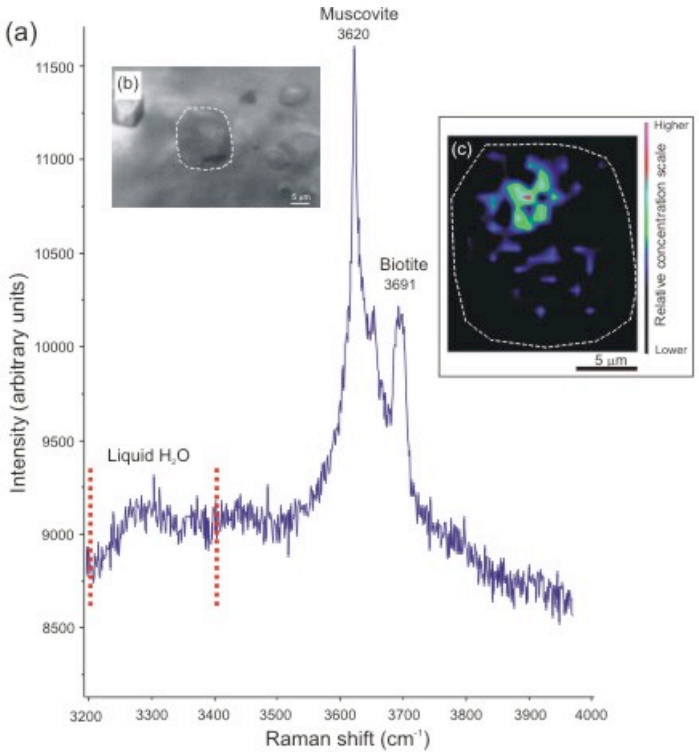

Fig. 9: Raman mapping of liquid H_2O distribution within a crystallized melt inclusion in metatexite. (a) Representative Raman spectrum obtained from mapping: the peaks at 3620 and 3691 cm^{-1} correspond to main OH stretching vibrations in muscovite and biotite, respectively. (b) Investigated inclusion below garnet surface. (c) Raman map in the 3200-3400 cm^{-1} stretching region (bounded by red dotted lines in a) of liquid H_2O. The inclusion contains both hydroxylated minerals and free H_2O in the pores.
Fig. 10: SEM-BSE images of MI in metatexite after remelting experiments at 700 °C (a) and 800 °C (b).

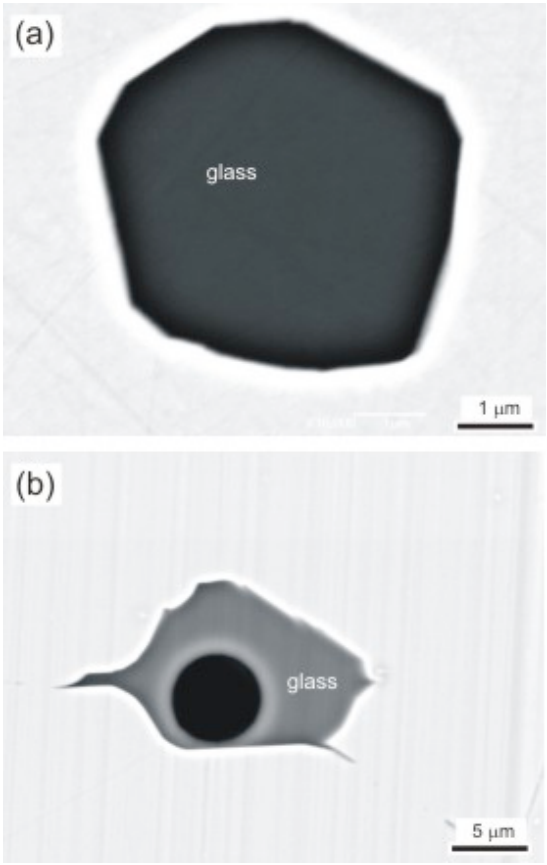

Fig. 10: SEM-BSE images of MI in metatexite after remelting experiments at 700 °C (a) and 800 °C (b).

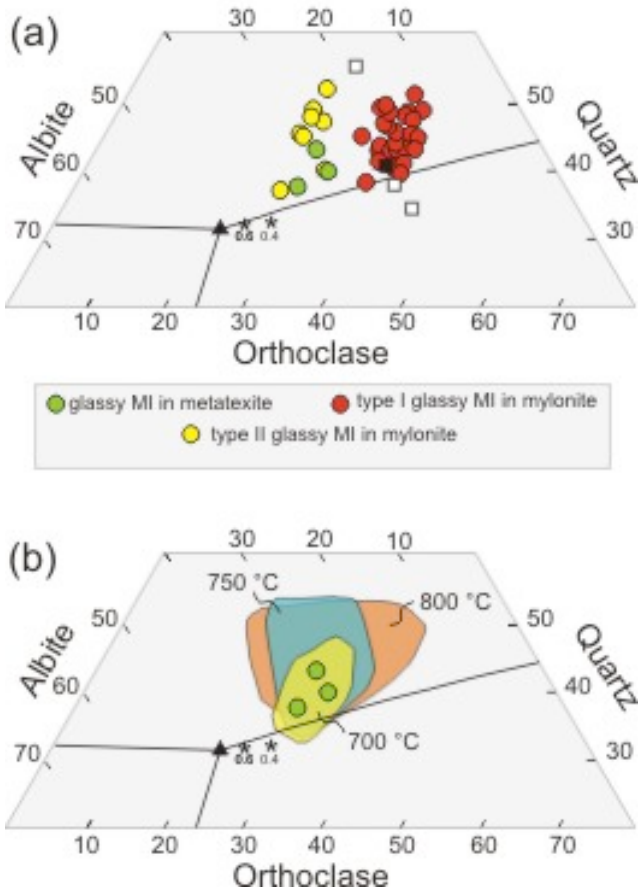

Fig. 11: CIPW normative compositions of glassy MI in metatexite and mylonite (a) and of re-melted MI in metatexite (b), shown on the Qtz-Ab-Or diagram. Compositions of leucosomes in metatexite (white squares) and mylonite (black square) are plotted for comparison. Data from dry and wet experiments overlap at 700, 750 and 800 °C (not shown; for details see Bartoli et al., 2013a). Black triangle and lines show eutectic point and cotectic lines for the subaluminous haplogranite system at 0.5 GPa and a_{H2O} = 1; black stars are eutectic points at a_{H2O} = 0.6 and 0.4 (Becker et al. 1998).

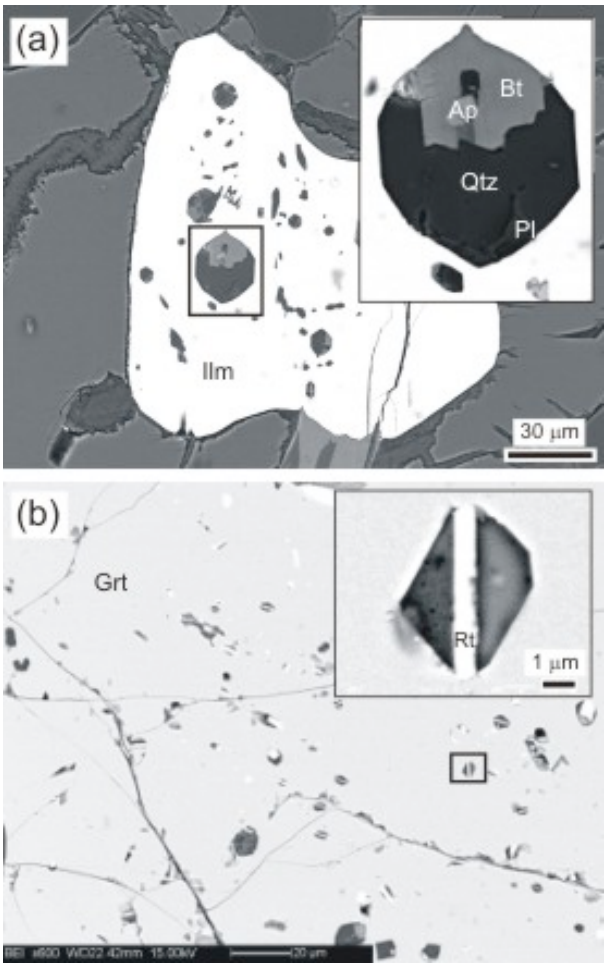

Fig. 12: (a) SEM-BSE image of an ilmenite crystal in the pelitic metatexite ALPA35-2, containing primary MI. (b) SEM-BSE image of rutile-bearing MI hosted in garnet of the pelitic granulite ALP14.

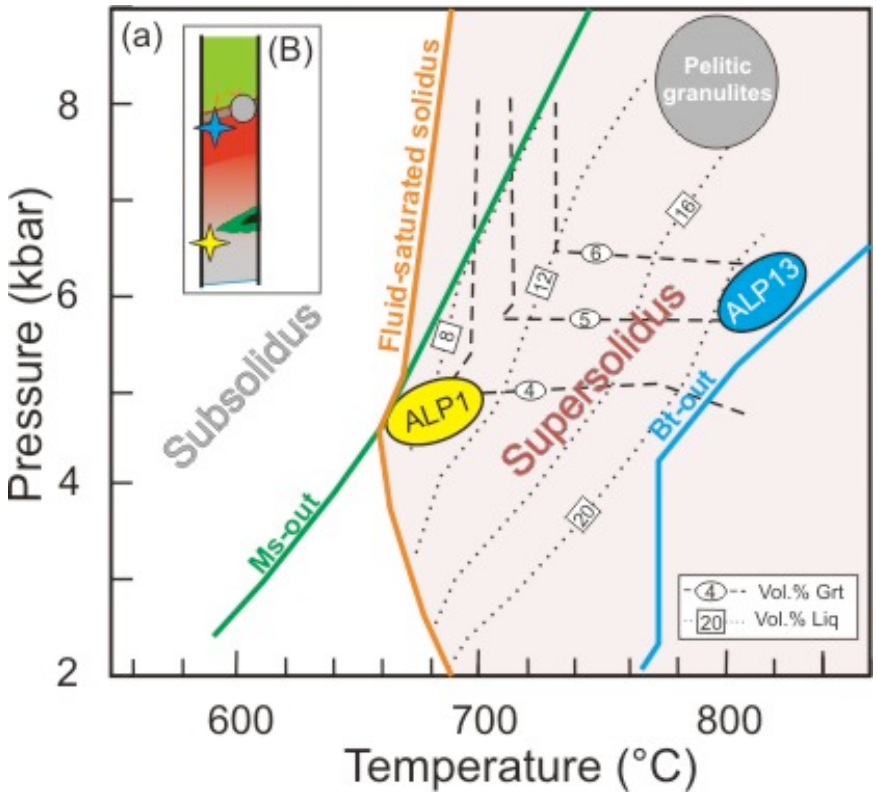

Fig. 13: Inferred P–T conditions of equilibration for the studied metatexite ALP1 and mylonite ALP13 (with data from Bartoli et al., 2013c). P–T estimates for pelitic granulites (i.e.rutile-bearing mylonites) are reported for comparison (data from Tubía et al., 1997). (b) Simplified section reported in Fig. 2, showing the relative stratigraphic position of the rocks reported in (a). See text for explanation.

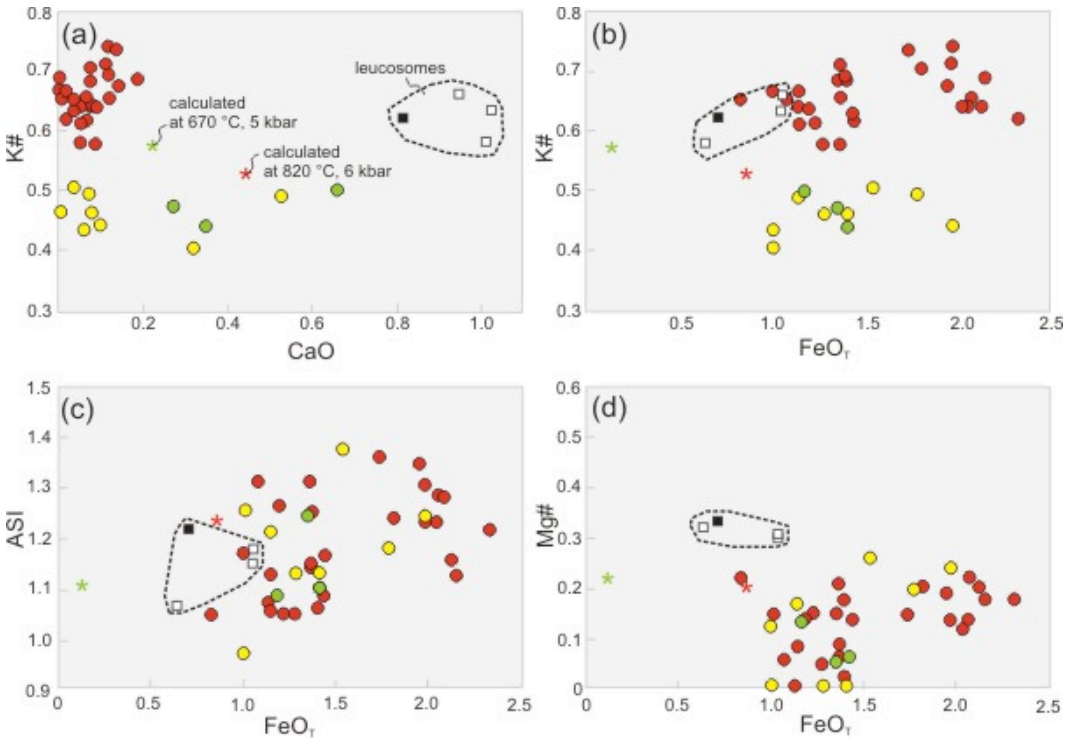

Fig. 14: Bivariant diagrams showing the compositions of MI and coexisting leucosomes. Symbols as in Fig. 11. The compositions calculated by thermodynamic modeling (red and green asterisks) are plotted for comparison. (a) CaO vs. K# [K# =mol. $K_2O/(Na_2O+K_2O)$]. (b) FeO_T vs. K# (with all iron treated as FeO and reported as FeO_T). (c) FeO_T vs. ASI [ASI = mol. $Al_2O_3/(CaO+Na_2O+K_2O)$]. (d) FeO_T vs. Mg# [Mg# =mol. $MgO/(FeO_t+MgO)$].

Table 1: Major element average composition (wt%) of glassy melt inclusions in metatexite ALP1 (data from Bartoli et al., 2013b) and mylonite ALP13, and of coexisting leucosomes (data from Bartoli, 2012). Numbers in parentheses refer to 1σ standard deviation.

	Melt inclusions						Leucosomes			
	Metatexite		Mylonite				Metatexite		Mylonite	
			Type I		Type II					
No. Analyses	*3*		*31*		*8*		*3*		*1*	
SiO_2	69.69	(1.76)	76.33	(1.48)	75.97	(2.20)	75.66	(3.74)	74.53	
TiO_2	0.08	(0.14)	0.05	(0.08)	0.07	(0.07)	0.13	(0.03)	0.07	
Al_2O_3	11.78	(0.32)	11.35	(0.53)	11.30	(0.73)	13.15	(2.09)	14.14	
FeO	1.2	(0.11)	1.60	(0.50)	1.34	(0.34)	0.91*	(019)	0.71*	
MnO	0.09	(0.09)	0.06	(0.06)	0.08	(0.08)	0.02	(0.00)	0.02	
MgO	0.07	(0.03)	0.17	(0.11)	0.15	(0.15)	0.24	(0.04)	0.21	
CaO	0.39	(0.19)	0.07	(0.04)	0.14	(0.17)	0.99	(0.04)	0.81	
Na_2O	3.09	(024)	1.96	(0.35)	3.05	(0.51)	2.19	(016)	2.32	
K_2O	4.19	(0.23)	5.76	(0.36)	3.98	(0.33)	5.68	(1.11)	5.83	
P_2O_5	0.18	(0.27)	0.23	(0.23)	0.29	(0.29)	0.13	(0.01)	0.13	
LOI							0.46	(0.07)	0.58	
Total	90.76	(1.61)	97.58	(1.60)	96.37	(1.08)	99.56	(0.17)	99.33	
ASI[a]	1.15	(0.09)	1.19	(0.10)	1.19	(0.12)	1.13	(0.05)	1.22	
Na_2O/K_2O	0.74	(0.09)	0.34	(0.06)	0.77	(0.11)	0.40	(0.06)	0.40	
K#[b]	0.47	(0.03)	0.66	(0.04)	0.46	(0.03)	0.63	(0.03)	0.62	
H_2O[c]	9.24	(1.61)	2.42	(1.60)	3.63	(1.08)				
Calculated normative mineralogy										
Qtz	34.23	(2.86)	41.26	(2.68)	41.56	(5.06)	39.07	(8.86)	37.09	
Crn	1.87	(0.63)	1.86	(0.89)	1.91	(1.02)	1.92	(0.72)	2.87	
Or	24.77	(1.34)	34.02	(2.15)	23.50	(1.95)	33.58	(6.57)	34.43	
Ab	26.11	(2.07)	16.56	(2.98)	25.84	(4.29)	18.53	(1.37)	19.60	
An	0.83	(0.72)	0.13	(0.22)	0.18	(0.23)	4.04	(0.23)	3.15	

[a]Alumina Saturation Index [= mol. $Al_2O_3/(CaO+Na_2O+K_2O)$]

[b]K# = mol. $K_2O/(Na_2O+K_2O)$

[c]H_2O content calculated by difference on the EMP total

* Fe as Fe_2O_3